Contents lists available at ScienceDirect

European Journal of Mechanics B/Fluids

Destabilising effects of plant flexibility in air and aquatic vegetation canopy flows

F. Gosselin, E. de Langre *

Département de Mécanique, LadHyX-CNRS, École Polytechnique, 91128 Palaiseau, France

ABSTRACT

With an analytical model coupling a mixing layer flow with an oscillating vegetation canopy through a drag force, we show that for both the cases of wind over a crop field and a water stream over aquatic plants, the dynamics of the plants is responsible for increasing the growth rate of the coupled instability in the lock-in range through two mechanisms. Because the flow and the vegetation canopy move in phase and thus minimise their interactions, the drag dissipation is decreased. The correlation between the two components of the perturbation flow velocity in the mixing layer is increased and makes the perturbation flow more efficient at extracting energy from the mean flow.

© 2008 Elsevier Masson SAS. All rights reserved.

1. Introduction

The focus of this paper is the strong coupling between the dynamics of a fluid flow such as the wind or water current and that of a plant canopy. By plant canopy, we mean a large collection of individual plants such as a dense forest, a crop field, or an aquatic plant cover. The perspective we take on the plants is focused on the canopy as a whole; we perceive the canopy as a poroelastic continuum [1].

Understanding the mechanisms of interactions between flow and a plant canopy is crucial in predicting and avoiding wind-induced damage to forest [2,3] and crops [4]. Such an understanding is also essential to properly model the heat, mass and momentum exchanges between plants and the atmosphere [5,6] or between aquatic plants and the water stream they thrive in [7]. Other motivations for pursuing research in this field relate to artistic rendering of realistic vegetation movements [8] and to predicting the mechanical stimulus of wind on plants which influences the growth of plants [9].

The structure of the wind over a vegetation canopy is dominated by a Kelvin–Helmholtz (KH) instability due to the difference of air velocity above and inside the canopy [10]. A similar phenomenon is observable in aquatic flows over fully-submerged vegetation [11]. The KH instability, which is due to the presence of an inflection point in the velocity profile [12], engenders coherent eddies of canopy scale which dominate the turbulent motion of the canopy flow. When the vegetation canopy is flexible, these coherent eddies are responsible for wavelike motions at the canopy top.

These wavelike motions are called honami on crop fields and monami on aquatic plants.

Py et al. [13] showed with on-site experiments using an image-correlation technique that honami occurs at the free-vibration frequency of the plants. They also proposed an analytical model which couples a mixing-layer flow with a vegetation canopy free to oscillate. The model for the oscillating canopy is inspired by those of Farquhar and Eggleton [14] and Doaré et al. [15], but the novelty comes from the fact that the forcing is not externally imposed. The movements of the canopy are coupled with the perturbation flow arising from the instability of the mean mixing-layer flow above the canopy. The two-dimensional conservation of momentum equations are coupled to the canopy oscillator equation through a drag term. This linear model predicts a lock-in mechanism similar in form, but different mechanically to what is observed in vortex-induced vibration [16]. As the mean mixing-layer flow velocity is increased from zero, its KH instability frequency increases and as it approaches the natural frequency of the plants, it deviates and locks onto it. In this lock-in range, the growth rate of the instability is significantly increased. By comparing their experimental observations and the theoretical predictions of their model, Py et al. [13] concluded that "it is thus the lock-in mechanism suggested by the analysis of the coupled model that explains why the coherent wave-motion of the crops occurs at their eigenfrequency independently of [the wind velocity]".

The aim of the present study is to understand the dynamical interactions between the mixing layer and the vegetation canopy through which the growth rate of the coupled system is increased. The best method to do this is to use a theory as simple as possible which models only the essential mechanisms governing the interactions between canopy and flow. We revisit the linear analytical model developed by Py et al. [13,17] which couples the oscillator equation of the crop canopy with a perturbed broken line hori-

* Corresponding author. Tel.: +33-1-69-33-52-67; fax: +33-1-69-33-52-92.
E-mail address: delangre@ladhyx.polytechnique.fr (E. de Langre).

Nomenclature

C	drag-to-shear ratio
$C_D d$	dimensional drag coefficient
C_{uv}	streamwise and vertical velocity correlation coefficient
$\langle C_{uq} \rangle$	height-averaged correlation coefficient of the canopy and fluid velocities
D_i	canopy-fluid interaction drag dissipation
E	perturbation kinetic energy density
F_R	Froude number
g	gravitational acceleration
H, H_b, ξ	total, mean and perturbation height of the fluid domain
h	canopy height
k	perturbation wavenumber
m	canopy modal mass
P, P_b, p	total, mean and perturbation pressure
P_s	energy production from the Reynolds stresses
Q, Q_b, q	total, mean and perturbation canopy modal deformation

R	shear parameter
t	time
U_R	reduced velocity
U_1, U_2	mean flow velocity above and within the canopy
V_x, U_b, u	total, mean and perturbation streamwise flow velocity
V_y, v	total, and perturbation vertical flow velocity
X	canopy deformation
x, y	streamwise and vertical position coordinates
ρ	fluid density
χ	canopy deformation mode
$\omega, \omega_r, \omega_i$	complex, real, and imaginary perturbation frequency
$\bar{}$	denotes a dimensionless variable
$*$	denotes the complex conjugate of the quantity it follows
$\hat{}$	denotes the t- and x-independent part of a travelling-wave solution

---

zontal wind profile through a drag force. We improve slightly the model by not requiring the irrotationality assumption in the flow solution and in order to broaden the applicability of the model, we account for the free surface in the case of submerged aquatic plants.

The article is organised as follows. In Section 2, the model is derived and the stability analysis is formulated. The perturbation kinetic energy method and the correlation concepts are also briefly recalled. In Section 3, the stability analysis is performed on two cases: wind on a crop field and shallow aquatic flow over submerged vegetation. In both cases the dynamics of the plants is responsible for increasing the growth rate of the coupled instability in the lock-in range through two mechanisms: increased correlation of the fluctuations and decrease of the drag dissipation. The independent study of each case is followed by a comparative analysis based on dimensionless numbers. The last results presented in Section 3 show that the increase of coherence in the mixing layer predicted by the model can be observed experimentally and that our analytical model can fairly predict the occurrence of monami in the experiments of Nepf and Vivoni [18] and Ghisalberti and Nepf [11] on flexible model aquatic plants. The main results of our study conclude the article in Section 4.

2. Methodology

2.1. Linear stability model

We revisit the linear analytical model developed by Py et al. [13] which couples a mixing-layer flow with an oscillating vegetation canopy through a drag force.

Let us consider the stability of a 2-dimensional inviscid and incompressible flow of fluid of density ρ over a uniform vegetation canopy of height h as depicted in Fig. 1. Its velocity and pressure fields, $\vec{V}(x, y, t)$ and $P(x, y, t)$, are governed by the Euler equations

$$\rho \left[\frac{\partial \vec{V}}{\partial t} + (\vec{V} \cdot \vec{\nabla}) \vec{V} \right] = -\vec{\nabla} P + \vec{f}, \tag{1}$$

$$\vec{\nabla} \cdot \vec{V} = 0, \tag{2}$$

where $\vec{f}$ is the external body force caused by every plant in the canopy and therefore depends on the movement of each individual plant. If we assume that the spacing between the plants ℓ is regular and small as compared to the length scale of the perturbations
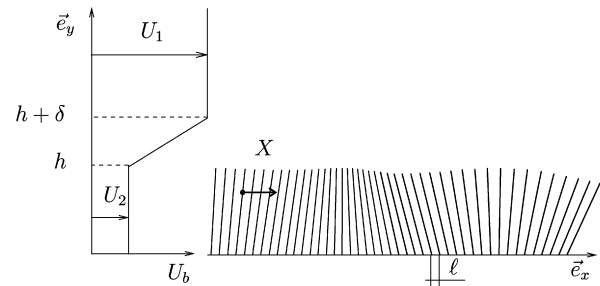

Fig. 1. Schematic of the modelled wind profile and crop canopy. Image reproduced from [13].

in the flow, we can treat the numerous plants as a continuum. Taking the horizontal displacement of the canopy as $X(x, y, t)$ we can write the body force acting on the fluid inside the canopy as

$$\vec{f} = -\frac{1}{2} \rho \frac{C_D d}{\ell^2} \left| V_x - \frac{\partial X}{\partial t} \right| \left(V_x - \frac{\partial X}{\partial t} \right) \vec{e}_x, \tag{3}$$

where $\vec{V} = (V_x, V_y)$ and where the product $C_D \times d$ is a dimensional drag coefficient assumed to be uniform along the plant height and independent of the flow velocity. Note that the diameter needs not to be defined, only the product $C_D d$ (see Py et al. [13]). This dimensional drag coefficient is set to zero outside the canopy ($y > h$). On the flow field, we apply the boundary conditions of no penetration at the ground and vanishing vertical velocity at infinite height, i.e.,

$$V_y|_{y=0} = 0, \qquad \lim_{H \to \infty} V_y|_{y=H} = 0. \tag{4}$$

In order to model the inflectional mean flow velocity profile in the framework of this linear analysis, we impose a basic flow $U_b(y)$ which takes the form of a piecewise linear velocity profile defined by a vorticity thickness δ and two velocities: U_1 above the mixing layer and U_2 inside the canopy (see Fig. 1).

To model the canopy motions, we use separation of variables $X(x, y, t) = \chi(y) Q(x, t)$ and consider only the fundamental mode of vibration of the plant stem $\chi(y) = y/h$. Here the fundamental mode is greatly simplified. Using a more realistic y-distribution for χ is not expected to alter the conclusions reached below for it is only a weight function for the drag term. Upon projection of this mode on the drag force acting on one plant, and upon neglecting

both structural damping and contact damping, we can write the equation governing the dynamics of the canopy as

$$m\frac{\partial^2 Q}{\partial t^2} + m\omega_0^2 Q = \int_0^h \frac{1}{2}\rho C_D d\left|V_x - \chi\frac{\partial Q}{\partial t}\right|\left(V_x - \chi\frac{\partial Q}{\partial t}\right)\chi\,\mathrm{d}y, \quad (5)$$

where ω_0 is the natural frequency of oscillation of the canopy and the modal mass is

$$m = \int_0^h m_i(y)\chi^2(y)\,\mathrm{d}y, \quad (6)$$

and where m_i is the mass distribution along the height of the plant. Up to here the derivation is identical, although organised differently, to [13], but to ease our analysis, we use a different non-dimensionalization. We define the mass number, the drag-to-shear ratio, the relative distance of the mixing layer from the ground, the shear parameter and the reduced velocity as

$$M = \frac{m}{\rho h \ell^2}, \quad C = \frac{C_D d\delta}{\ell^2}(1 - R), \quad \bar{h} = \frac{h}{\delta},$$

$$R = \frac{U_1 - U_2}{U_1 + U_2}, \quad U_R = \frac{U}{\delta\omega_0}, \quad (7)$$

as well as the following quantities

$$\bar{t} = t\frac{U}{\delta}, \quad \bar{x} = \frac{x}{\delta}, \quad \bar{y} = \frac{y}{\delta}, \quad \bar{Q} = \frac{Q}{\delta},$$

$$\bar{U}_b = \frac{U_b}{U}, \quad \bar{V}_x = \frac{V_x}{U}, \quad \bar{V}_y = \frac{V_y}{U}, \quad \bar{P} = \frac{P}{\rho U^2}, \quad (8)$$

where $U = (U_1 + U_2)/2$ is the average velocity. To investigate the stability of a given basic state composed of a basic horizontal velocity $\bar{U}_b$, pressure $\bar{P}_b$ and the corresponding equilibrium modal deformation of the canopy $\bar{Q}_b$, we introduce the associated small perturbations $\bar{u}$, $\bar{v}$, $\bar{p}$, and $\bar{q}$. Once we make the conservation of momentum, conservation of mass and the oscillator equations (1), (2), (5) dimensionless we can substitute the perturbation scheme while keeping only first order quantities to obtain

$$\frac{\partial \bar{u}}{\partial \bar{t}} + \bar{U}_b\frac{\partial \bar{u}}{\partial \bar{x}} + \bar{v}\frac{\partial \bar{U}_b}{\partial \bar{y}} = -\frac{\partial \bar{p}}{\partial \bar{x}} - C\left(\bar{u} - \chi\frac{\mathrm{d}\bar{q}}{\mathrm{d}t}\right), \quad (9)$$

$$\frac{\partial \bar{v}}{\partial \bar{t}} + \bar{U}_b\frac{\partial \bar{v}}{\partial \bar{x}} = -\frac{\partial \bar{p}}{\partial \bar{y}}, \quad (10)$$

$$\frac{\partial \bar{u}}{\partial \bar{x}} + \frac{\partial \bar{v}}{\partial \bar{y}} = 0, \quad (11)$$

$$\frac{\partial^2 \bar{q}}{\partial \bar{t}^2} + U_R^{-2}\bar{q} = \frac{C}{M\bar{h}}\int_0^{\bar{h}}\left(\bar{u} - \chi\frac{\partial \bar{q}}{\partial \bar{t}}\right)\chi\,\mathrm{d}\bar{y}, \quad (12)$$

where we recall that in Eq. (9), C is zero outside the canopy ($\bar{y} > \bar{h}$). We seek a solution to Eqs. (9)–(12) in the form of a travelling wave

$$(\bar{u}, \bar{v}, \bar{p}, \bar{q}) = (\hat{u}, \hat{v}, \hat{p}, \hat{q})\,\mathrm{e}^{i(\bar{k}\bar{x} - \bar{\omega}\bar{t})} + \text{c.c.}, \quad (13)$$

where $\bar{k}$ and $\bar{\omega}$ are the dimensionless axial wavenumber and complex frequency and where c.c. stands for complex conjugate.

Upon substitution of the travelling-wave solution in Eqs. (9)–(11), we can solve analytically for the general shape functions of the vertical velocity and pressure fields in the domain (see Appendix A). From this general flow solution continuous on the $\bar{y}$-domain, we can obtain the particular solution by imposing that it respects the travelling-wave form of the boundary conditions equations (4) and oscillator equation (12). We write these 7 conditions (see Appendix A) on the general solution as a linear operator

$$\left[\mathbf{L}(U_R, C, M, R, \bar{h}, \bar{\omega}, \bar{k})\right]\{\vec{A}\} = \{0\}, \quad (14)$$

where $\vec{A}$ represents the 7 integration constants of the general shape functions. We obtain the dispersion relation of the admissible complex frequencies $\bar{\omega}$ with the wavenumbers $\bar{k}$ by taking the determinant of $\mathbf{L}$ equal to zero. For a given value of $\bar{k}$, the corresponding complex values of $\bar{\omega}$ are found with a Müller iterative procedure. Each combination of $\bar{k}$ and $\bar{\omega}$ solving the governing equations of the system corresponds to a mode of the system. For each mode, the complex frequency has a real and an imaginary part, $\bar{\omega} = \bar{\omega}_r + i\bar{\omega}_i$. The real part is the frequency of oscillation and the imaginary part is the growth rate. If $\bar{\omega}_i > 0$, the mode of vibration is unstable and a small perturbation will increase exponentially. On the other hand, if $\bar{\omega}_i < 0$, the mode of vibration is stable and a small perturbation will decay. If $\bar{\omega}_i = 0$, the mode is neutrally stable.

In [13], to simplify the analytical flow solution and obtain a dispersion relation in the form of a polynomial of $\bar{\omega}$, the flow was assumed irrotational although the canopy drag is clearly dissipative. Because of that assumption, their flow solution did not respect the governing Euler equations. We show in Appendix A that this assumption is not necessary and in Section 3.1, we show that the effect of this assumption on the dynamics of the system is quantitative but not qualitative.

2.2. Free surface

In order to broaden the applicability of the coupled model to the case of shallow aquatic flow over vegetation, we introduce the free surface boundary conditions. At the ground, we keep the no penetration condition as in Eqs. (4), but at height $H(x, t)$ we impose a free surface [19], i.e.,

$$V_y|_{y=0} = 0, \quad V_y|_{y=H} = \frac{\mathrm{D}H}{\mathrm{D}t}, \quad \text{and} \quad P|_{y=H} = 0, \quad (15)$$

where $\mathrm{D}/\mathrm{D}t$ is the Lagrangian derivative. We define the dimensionless height $\bar{H} = H/\delta$ and expand it into a mean and a fluctuating heights $\bar{H}(\bar{x}, \bar{t}) = \bar{H}_b + \bar{\xi}(\bar{x}, \bar{t})$. With the mean height and the gravitational acceleration g, we define the Froude number $F_R = \sqrt{U^2/gH_b}$ to make Eqs. (15) dimensionless. The resulting equations can then be approximated at the instantaneous position of the surface via a Taylor expansion and keeping only first order terms:

$$\bar{v}|_{\bar{y}=0} = 0, \quad \bar{v}|_{\bar{y}=\bar{H}_b} = \frac{\partial \bar{\xi}}{\partial \bar{t}} + (1 + R)\frac{\partial \bar{\xi}}{\partial \bar{x}}, \quad \text{and}$$

$$\bar{p}|_{\bar{y}=\bar{H}_b} = \frac{1}{\bar{H}_b F_R^2}\bar{\xi}. \quad (16)$$

Assuming that the free-surface waves take a travelling-wave form similar to Eq. (13), i.e. $\bar{\xi}(\bar{x}, \bar{t}) = \hat{\xi}\,\mathrm{e}^{i(\bar{k}\bar{x} - \bar{\omega}\bar{t})} + \text{c.c.}$, the boundary conditions of Eq. (16) can be written as

$$\hat{v}|_{y=0} = 0, \quad \hat{v}|_{\bar{y}=\bar{H}_b} = i\bar{H}_b\bar{k}F_R^2\left(1 + R - \frac{\bar{\omega}}{k}\right)\hat{p}|_{\bar{y}=\bar{H}_b}. \quad (17)$$

To model shallow aquatic flow over vegetation, Eqs. (17) are used in the system of Eqs. (14) instead of the semi-infinite domain boundary conditions.

Once the frequency and wavenumber are obtained by solving the system of Eqs. (14) with the Müller iterative procedure, we can substitute them back in the particular shape functions of the velocity and pressure fields to get an insight of the flow behaviour. This insight is further improved by examining the perturbation flow energy and correlations obtained in the next subsections.

2.3. Energy considerations

We apply the energy method described by Drazin and Reid [19, p. 424] and applied by Cossu and Brandt [20] to investigate the energy production and dissipation in the perturbation fluid flow.

The perturbation kinetic energy density in the fluid, $e = \frac{1}{2}(\bar{u}^2 + \bar{v}^2)$, is averaged over one wavelength $\lambda = 2\pi/\bar{k}$ and summed over the height of the domain $\bar{H}_b$:

$$E = \frac{1}{\lambda} \int_0^{\bar{H}_b} \int_0^\lambda (\bar{u}^2 + \bar{v}^2) \, d\bar{x} \, d\bar{y}. \tag{18}$$

We are interested in the change over time of the averaged perturbation kinetic energy density

$$\frac{\partial E}{\partial \bar{t}} = \frac{1}{\lambda} \int_0^{\bar{H}_b} \int_0^\lambda \left(\bar{u} \frac{\partial \bar{u}}{\partial \bar{t}} + \bar{v} \frac{\partial \bar{v}}{\partial \bar{t}} \right) d\bar{x} \, d\bar{y}, \tag{19}$$

which is obtained by multiplying the linearised equations of motion of the fluid (9)–(10) by u and v respectively. Upon integration, the divergence terms give a zero global contribution term to the energy balance and we are left with the following non-null terms

$$\frac{\partial E}{\partial \bar{t}} = P_s - D_i - S_f, \tag{20}$$

where P_s is the energy production from the Reynolds stresses, D_i is the drag dissipation due to the interaction of the wind with the canopy and S_f is the storage of energy in the deformation of the free surface, i.e.,

$$P_s = -\frac{1}{\lambda} \int_{\bar{h}}^{\bar{h}+1} \int_0^\lambda \bar{u} \bar{v} \frac{\partial \bar{U}_b}{\partial \bar{y}} \, d\bar{x} \, d\bar{y}, \tag{21}$$

$$D_i = \frac{1}{\lambda} \int_0^{\bar{h}} \int_0^\lambda C \left(\bar{u}^2 - \bar{u} \chi \frac{\partial \bar{q}}{\partial \bar{t}} \right) d\bar{x} \, d\bar{y}, \tag{22}$$

$$S_f = \frac{1}{\lambda} \int_0^{\bar{H}_b} \int_0^\lambda \frac{\partial}{\partial \bar{y}} (\bar{v}\bar{p}) \, d\bar{x} \, d\bar{y}. \tag{23}$$

Notice that the drag dissipation is composed of two terms: a positive one proportional to the square of the horizontal perturbation velocity inside the canopy and one which may be positive or negative depending on the phase between the fluid ans the solid motions. The energy quantities vary in time as $(E, P_s, D_i, S_f) = (\hat{E}, \hat{P}_s, \hat{D}_i, \hat{S}_f)e^{2\bar{\omega}_i \bar{t}}$ and using the travelling-wave solution form, Eqs. (18), (21)–(23) can be rewritten as

$$\hat{E} = \int_0^{\bar{H}_b} (\hat{u}\hat{u}^* + \hat{v}\hat{v}^*) \, d\bar{y}, \tag{24}$$

$$\hat{P}_s = -\int_{\bar{h}}^{\bar{h}+1} (\hat{u}\hat{v}^* + \hat{u}^*\hat{v}) \frac{\partial \bar{U}_b}{\partial \bar{y}} \, d\bar{y}, \tag{25}$$

$$\hat{D}_i = \int_0^{\bar{h}} C[2\hat{u}\hat{u}^* + i\bar{\omega}\chi\hat{q}\hat{u}^* - i\bar{\omega}^*\chi\hat{q}^*\hat{u}] \, d\bar{y}, \tag{26}$$

$$\hat{S}_f = [\hat{v}^*\hat{p} + \hat{v}\hat{p}^*]_{\bar{y}=\bar{H}_b}, \tag{27}$$

where * denotes the complex conjugate of the quantity it follows. Note that the energy storage by the free surface deformation $\hat{S}_f$ is null when the boundary condition of vanishing vertical velocity at infinite height (Eqs. (4)) is considered. The following identity is immediately derived from Eq. (20):

$$\bar{\omega}_i = \frac{\hat{P}_s}{2\hat{E}} - \frac{\hat{D}_i}{2\hat{E}} - \frac{\hat{S}_f}{2\hat{E}}, \tag{28}$$

similarly to what [19] and [20] obtained.

2.4. Correlations

To further analyse the results obtained with the linear model, we make use of correlation coefficients (see Tennekes and Lumley [21], Raupach et al. [10]). To study turbulent flows, use if often made of the streamwise and vertical fluctuation correlation coefficient

$$\tilde{C}_{uv} = \frac{\overline{u'v'}}{(\overline{u'^2}\,\overline{v'^2})^{1/2}}, \tag{29}$$

where u', v' are the streamwise and vertical turbulent fluctuations and where here the overbar denotes a time-average. In the framework of this modal analysis, the streamwise and vertical velocity correlation coefficient writes as

$$C_{uv}(\bar{y}) = \frac{\hat{u}\hat{v}^* + \hat{u}^*\hat{v}}{2\sqrt{\hat{u}\hat{u}^*\hat{v}\hat{v}^*}}, \tag{30}$$

and is independent of $\bar{x}$ or $\bar{t}$ without the use of averaging. Similarly, we can obtain the height-averaged correlation coefficient of the velocity of the canopy and the horizontal fluid velocity:

$$\langle C_{uq} \rangle = \int_0^{\bar{h}} \frac{\hat{u}(-i\bar{\omega}\chi\hat{q})^* + \hat{u}^*(-i\bar{\omega}\chi\hat{q})}{2\sqrt{\hat{u}\hat{u}^*(-i\bar{\omega}\chi\hat{q})(-i\bar{\omega}\chi\hat{q})^*}} \, d\bar{y}. \tag{31}$$

3. Results

3.1. Irrotationality

Before performing our analysis on the effect of vegetation on canopy flows, we want to assess the influence of the irrotational flow assumption made by Py et al. [13]. We use the data on wheat provided by Py et al. [13] which correspond to the dimensionless numbers given in Table 1 except for $R = 0.5$ and $\bar{h} = R^{-1}$. The complex frequency of the most unstable wavenumber for increasing reduced velocity is shown in Fig. 2 as obtained with our model and with the model of Py et al. [13] which assumes the flow irrotational. The behaviour is the same in both cases: at small and large reduced velocities, the complex frequency is relatively constant with U_R, but for a reduced velocity around 1, the frequency of the instability deviates and the growth rate increases. On the other hand, there is a significant quantitative difference between the predictions of the two models. The irrotational assumption causes the model to exaggerate the reduced velocity range over which the $\bar{\omega}_r$ deviates from its low U_R value and significantly underestimates
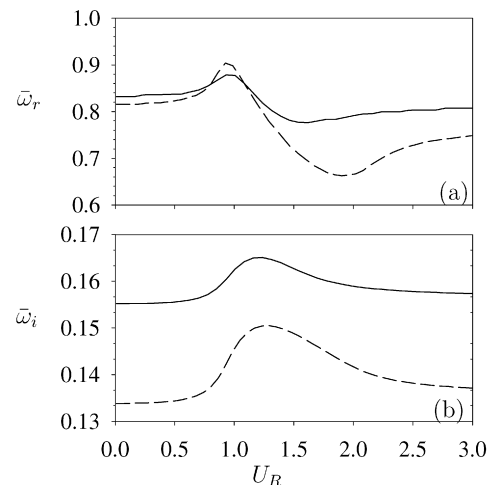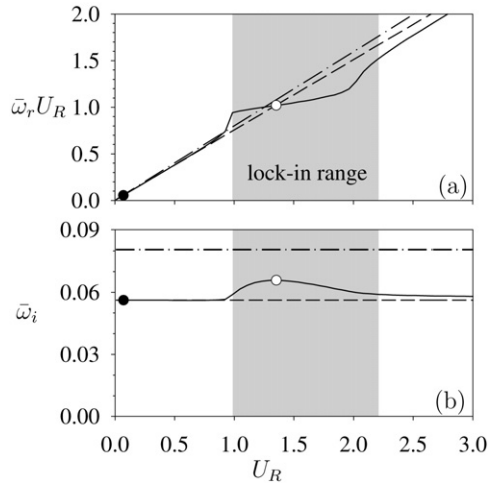
Fig. 2. Frequency evolution of the most unstable wavenumber computed with our model (—); with the irrotationality assumption (− − −).

Table 1
Values of the dimensionless parameters used in the simulations

	Crop canopy	Aquatic vegetation
M	0.74	0.0076
C	0.30	0.55
$\bar{h}$	5	0.36
R	0.2	0.55
$\bar{H}_b$	∞	15
$F_R U_R^{-1}$	N/A	0.07

Fig. 3. Frequency (a) and growth rate (b) of the wind-crop system: the pure configuration (−·−·); the heavy configuration (− − −); the coupled configuration (−). The grey area marks the lock-in range. The black and white dots correspond to the cases $U_R = 0.07$ and $U_R = 1.35$ studied in Figs. 4, 5 and 8.

the growth rate. By making this simplifying assumption in their model, Py et al. [13] added quantitative imprecision to their predictions but this did not influence qualitatively the mechanisms and interactions they predicted. In what follows in this article, all the results are obtained without making any assumption regarding the irrotationality of the flow.

3.2. Wind on a crop field

The model described in the previous section is used to investigate the instability mechanisms in the interactions between wind and a crop canopy. The parameters kept constant in this analysis are given in Table 1. All values are taken from the wind-wheat system of [13] except the value of R which is taken smaller here to amplify the coupling effects; yet it is still in the physically reasonable range considering the very coarse approximation a broken-line profile represents of a real wind profile. As in [13], we take $\delta = Rh$.

We study the evolution of the temporal stability of the system with increasing reduced velocity U_R in three configurations: the "coupled configuration" where the Kelvin–Helmholtz (KH) instability in the flow interacts with the flexible plant canopy, the "pure configuration" where a pure KH instability develops in a flow without vegetation as C is taken vanishingly small, and a "heavy configuration" where a KH instability develops over non-moving vegetation as M is taken very large. For every value of U_R, the most unstable wavenumber of each scenario is considered, i.e., the wavenumber which leads to the frequency with the most positive imaginary part $\bar{\omega}_i$.

The frequency of the pure configuration shown in dash-dot line in Fig. 3(a) is known to increase proportionally to the flow velocity [12]. Its growth rate, shown in Fig. 3(b), is constant with flow velocity. The frequency of the heavy configuration, in dash line in

Fig. 3(a), is smaller than that of the pure configuration. In the case of the coupled configuration (solid line in Fig. 3), for small and large reduced velocity, the frequency and the growth rate match those of the heavy configuration. This is so because the natural frequency of the plants and that of the KH instability then differ greatly, hence decoupling their dynamics. For the reduced velocity range corresponding to the grey area in Fig. 3, the frequency of the pure KH instability is closer to the natural frequency of the oscillating canopy and frequency lock-in occurs. As explained by Py et al. [13], "in this range the frequency of the instability locks onto the frequency of the plants as its value approaches and follows that of the plants." This leads to an increase in the instability, which can be visualised as a bump in the imaginary frequency plotted in solid line Fig. 3(b). This imaginary frequency grows larger, yet it remains smaller than that of the pure configuration. It is from the increase of the imaginary frequency that we define the lock-in range. The range of reduced velocity where the growth rate of the coupled system is increased by an arbitrary amount ϵ as compared to the heavy configuration ($\bar{\omega}_i|_{\text{coupled}} > \bar{\omega}_i|_{\text{heavy}} + \epsilon$) is here termed the lock-in range. In order to compare the wind-crop and the aquatic plant systems, we adopt a value of $\epsilon = 0.003$.

We now compare the perturbation solution at a small reduced velocity $U_R = 0.07$ marked out with the black dot in Fig. 3 to that at the reduced velocity maximising the growth rate $U_R = 1.35$ marked out with the white dot in Fig. 3. The analytical flow solutions of Eqs. (A.1)–(A.6) can easily be integrated to obtain the streamfunction of the perturbation flow. The streamlines along with the velocity of the crops $\partial \bar{q}/\partial t$ at $\bar{y} = \bar{h}$ over half a wavelength are plotted for $U_R = 0.07$ in Fig. 4 and $U_R = 1.35$ in Fig. 5. The velocities are normalised such that the total perturbation kinetic energy of the fluid over a wavelength is unity and such that the vertical velocity $\bar{v}$ at $\bar{y} = \bar{h}$ is maximised at $\bar{x} = 0$.

In Figs. 4, 5, there are three points to notice in comparing the perturbation solution at low reduced velocity to that maximising the growth rate: (i) the phase difference between the horizontal velocity of the fluid inside the canopy and that of the vegetation, (ii) the amplitude of the canopy motion $\partial \bar{q}/\partial \bar{t}$, and (iii) the magnitude of the velocity inside the canopy. (i) In Fig. 4, the maximum in the horizontal fluid velocity inside the canopy occurs around $\bar{x} = \pi/2\bar{k}$ while this coincides with a null velocity of the vegetation $\partial \bar{q}/\partial \bar{t}$. On the other hand, in Fig. 5, the maximum horizontal fluid velocity inside the canopy is close in space to that of the vegetation, around $\bar{x} = \pi/2\bar{k}$ where the streamlines are closest and most horizontal. As the reduced velocity is increased from 0.07 to 1.35 the motion of the plants and the fluid get in phase. This is better seen in Fig. 6(a) where is plotted the height-averaged correlation coefficient between the vegetation velocity and the horizontal flow velocity obtained in Eq. (31). Worth -0.2 at $U_R = 0$ the correlation increases sharply at $U_R = 1$ to peak just short of a perfect correlation at $U_R = 1.47$ and decline outside the lock-in range. (ii) This increase in the coherence between the motion of the vegetation and that of the fluid has for effect to increase the amplitude of $\partial \bar{q}/\partial \bar{t}$ by more than three orders of magnitude between $U_R = 0.07$ and $U_R = 1.35$ for the same perturbation flow energy in Figs. 4, 5. The motion of the plants becomes much more important in the dynamics of the system. (iii) In Fig. 5, the streamlines inside the canopy are closer to one another and more numerous than in Fig. 4. This indicates that for the same kinetic energy of the perturbation flow, the flow inside the canopy is faster at $U_R = 1.35$ than at $U_R = 0.07$. This increase of the flow velocity inside the canopy can be visualised in Fig. 6(b). We see that the percentage of all the fluid perturbation kinetic energy which is located inside the canopy increases from 18% to 23% as the reduced velocity increases from 0 to 1. This is just short of the 25% of the pure configuration. The steep increase of the percentage of the kinetic
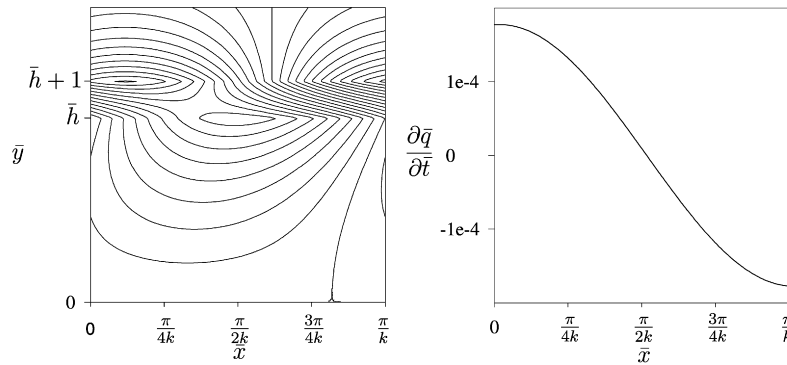
Fig. 4. Streamlines of the wind and velocity of the crops at $\bar{y} = \bar{h}$ over half a wavelength for $U_R = 0.07$ (outside lock-in).
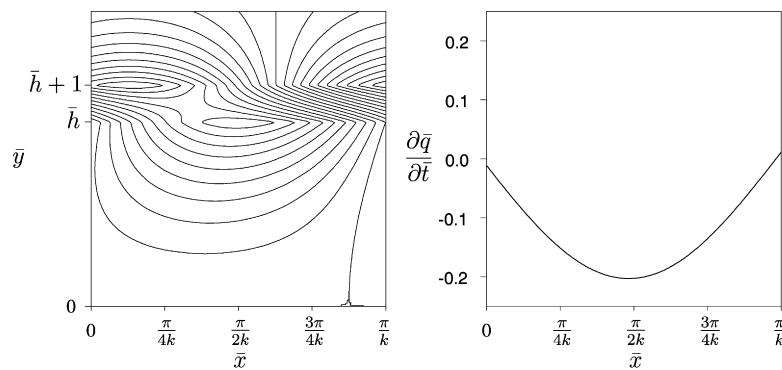

Fig. 5. Streamlines of the wind and velocity of the crops at $\bar{y} = \bar{h}$ over half a wavelength for $U_R = 1.35$ (within lock-in).
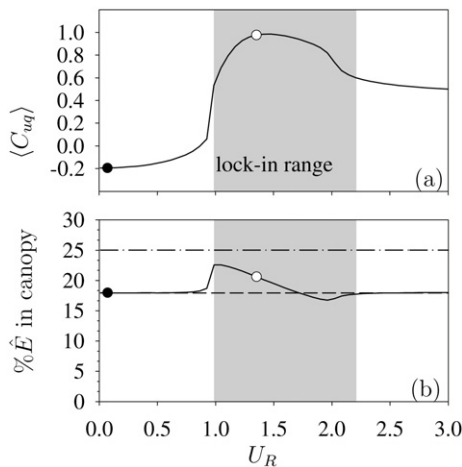

Fig. 6. Correlation of the horizontal wind and canopy velocities and percentage of the fluid perturbation kinetic energy inside the canopy for increasing reduced velocity in the wind-crop system: the pure configuration (–·–·); the heavy configuration (– – –); the coupled configuration (—). The grey area marks the lock-in range. The black and the white dots correspond to the cases $U_R = 0.07$ and $U_R = 1.35$ studied in Figs. 4, 5 and 8.

energy inside the canopy matches the increase of the correlation between the motion of the plants and the flow in Fig. 6(a).

The instability, which is almost entirely confined to the fluid part of the system at low reduced velocity, spreads to both the fluid and the oscillating canopy in the lock-in range. As a result the dynamics of the plants is responsible for increasing the rate of growth of the instability. This is shown by considering the perturbation energy production and dissipation in the system. The growth rate in solid line, along with the two terms accounting for it in Eq. (28) are plotted in Fig. 7: the production of kinetic energy by the work of the Reynolds stress against the shear
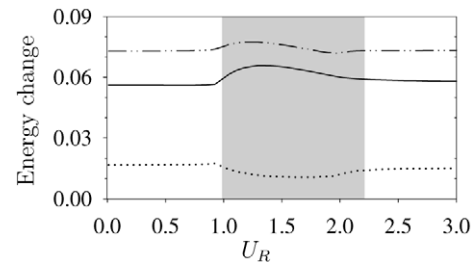

Fig. 7. Energy analysis of the coupled configuration for the wind-crop system: $\hat{D}_i/2\hat{E}$ (·····); $\hat{P}_s/2\hat{E}$ (–··–··); $\bar{\omega}_i$ (—). The grey area marks the lock-in range.

($\hat{P}_s/2\hat{E}$) in dash-dot-dot line and the drag dissipation ($\hat{D}_i/2\hat{E}$) in dotted line. Note that the term accounting for the energy storage by the free surface $\hat{S}_f$ vanishes for the wind-crop system. The Reynolds stresses extract energy from the shear of the basic flow and thus fuel the instability [19]. In a real canopy flow the wake of the plants takes energy from large-scale turbulent structures to feed smaller-scale turbulence hence short-circuiting the Kolmogorov cascade [6], but in the current perturbation-method study, canopy drag acts as pure dissipation to the perturbation flow.

The intensification of the production of perturbation kinetic energy with increasing U_R is caused by more coherence in the mixing layer $\bar{h} < \bar{y} < \bar{h} + 1$. The distribution with height of the correlation coefficient of the streamwise and vertical perturbation velocities $-C_{uv}(\bar{y})$ obtained in Eq. (30) is plotted in Fig. 8 for a case with small reduced velocity ($U_R = 0.07$ in dash line) and one maximising the growth rate ($U_R = 1.35$ in solid line). The increase in reduced velocity has a noticeable effect on the coefficient inside the canopy but the effect of importance is inside the shear layer. For the most part of $\bar{h} < \bar{y} < \bar{h} + 1$, the magnitude of $C_{uv}(\bar{y})$ is increased slightly by the motion of the canopy. The rise with U_R in the correlation between the streamwise and vertical perturba-
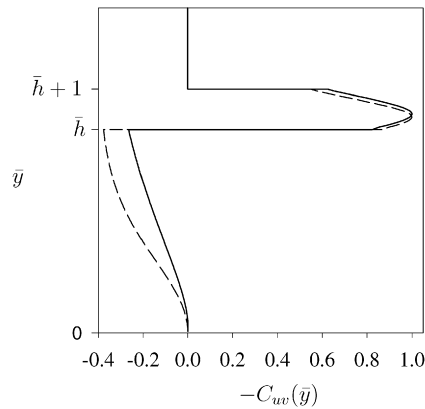
Fig. 8. Height distribution of the correlation coefficient of the streamwise and vertical perturbation velocities in the crop system for two cases: low reduced velocity, $U_R = 0.07$ (– – –); in the lock-in range, $U_R = 1.35$ (—).
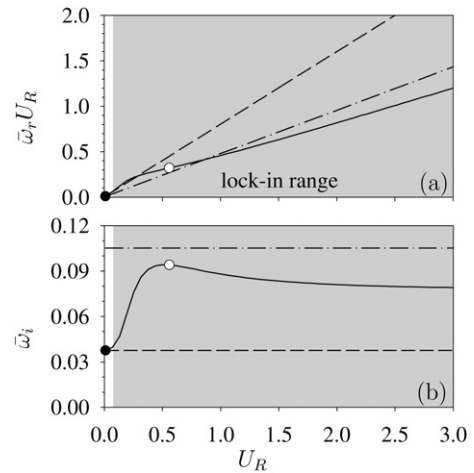

Fig. 9. Frequency (a) and growth rate (b) of the aquatic plant system: the pure configuration (– · – ·); the heavy configuration (– – –); the coupled configuration (—). The grey area marks the lock-in range. The black and the white dots correspond to the cases $U_R = 0.01$ and $U_R = 0.56$ studied in Figs. 10, 11 and 14.

tion velocity components has for effect to make the perturbation flow more effective at extracting energy from the mean flow and thus causes the small boost in energy production $\hat{P}_s/2\hat{E}$ as seen in Fig. 7. On the other hand, the decrease of the dissipation $\hat{D}_i/2\hat{E}$ in Fig. 7 is due to the fluid inside the canopy and the vegetation moving in phase with one another, i.e. it is due to the increased height-averaged correlation coefficient $\langle \bar{C}_{uq} \rangle$ with U_R shown in Fig. 6(a).

It is understood that as the reduced velocity enters the lock-in range, the most unstable perturbation mode reorganises such that the instability spreads to both the fluid and the oscillating canopy. As the canopy oscillates in phase with the flow, the drag dissipation of kinetic energy is reduced and the work of the Reynolds stresses against the mean flow shear is increased. These two canopy-flow interaction mechanisms contribute to making the system more unstable.

3.3. Shallow aquatic flow over submerged vegetation

Ghisalberti and Nepf [11] identified the mechanism of monami generation in shallow aquatic flow over submerged vegetation as the same mechanism responsible for honami on crops, namely the stream of coherent vortices produced by the KH instability in the mean flow. Since the same mechanism is responsible for the waving of plants in both systems, we could think that, as is shown to be the case for the wind-crop system in Subsection 3.2, the dynamics of the aquatic plant canopy is responsible for decreasing the stability of the water flow by diminishing the drag dissipation and augmenting the work of the Reynolds stresses in the lock-in velocity range. To verify this we use the same approach to investigate the interactions between a shallow water flow and submerged vegetation as in the previous subsection.

The model of Section 2 with the boundary conditions of Eqs. (17) is applied and the values given to the parameters are shown in Table 1. These parameter values are inspired by the model vegetation made of low density polyethylene film of Ghisalberti and Nepf [11]. Their model plants were shown to exhibit realistic aquatic plant dynamics in flume experiments and all their characteristics are known. In calculating the mass per unit length and the natural frequency of the aquatic plants to use in our model, the added mass and the buoyancy effect are taken into account (see Appendix B). A broken-line velocity profile is fitted on the hyperbolic velocity profile experimentally measured in the scenario A of Ghisalberti and Nepf by imposing three similarity conditions (see Appendix B). To simplify the analysis and minimise the influence of free-surface waves on the dynamics, the height of the free surface H_b in the simulations of this subsection is taken

larger than in the experiments of [11] so as to keep the Froude number low. The maximum value of the Froude number reached in the simulations here is $F_R = 0.21$. As in Subsection 3.2 we consider the three configurations: coupled, pure and heavy.

The evolutions with flow velocity of the frequencies and growth rates of the three configurations are plotted in Fig. 9. For very small reduced velocities, the frequency of the coupled configuration follows that of the heavy configuration, but as U_R is increased to a value larger than 0.2, lock-in occurs and the growth rate climbs. The lock-in range, defined as the reduced velocity range where $\bar{\omega}_i|_{coupled} > \bar{\omega}_i|_{heavy} + \epsilon$ and identified by the area in grey in Fig. 9, begins at a very small reduced velocity and a frequency only a fraction of the natural frequency of the aquatic plants. Note that as in the wind-crop system, a value of $\epsilon = 0.003$ is used. We still call it "lock-in" even though it does not occur around the natural frequency of the aquatic plants because, as is shown in the following lines, it is still the same mechanisms that are responsible for destabilising further the system.

The lock-in range and its increase of the growth rate are accompanied with significant changes in the dynamics of the perturbation solution. The velocity of the vegetation $\partial \bar{q}/\partial t$ at the top of the canopy $\bar{y} = \bar{h}$ along with the streamlines of the perturbation flow over half a wavelength are shown in Fig. 10 for a case of low reduced velocity ($U_R = 0.01$ marked out with the black dot in Fig. 9) and in Fig. 11 for a case at the peak of the growth rate ($U_R = 0.56$ marked out with the white dot in Fig. 9). The velocities are normalised such that the total perturbation kinetic energy of the fluid over a wavelength is unity and such that the vertical velocity $\bar{v}$ at $\bar{y} = \bar{h}$ is maximised at $\bar{x} = 0$.

As in the wind-crop analysis, when comparing the perturbation solutions at low reduced velocity and at the reduced velocity maximising the growth rate in Figs. 10, 11 there are three important differences to notice: (i) the phase difference between the horizontal velocity of the fluid inside the canopy and the velocity of the vegetation, (ii) the amplitude of the canopy motion $\partial \bar{q}/\partial \bar{t}$, and (iii) the magnitude of the velocity inside the canopy. (i) In Fig. 10, the fluid horizontal velocity is out of phase with the vegetation velocity. In Fig. 11, they are in phase: notice the streamlines inside the canopy are closest and all horizontal at $\bar{x} = \pi/2\bar{k}$ while this coincides with a peak of $\partial \bar{q}/\partial \bar{t}$. In the lock-in range, the motion of the plants and the fluid get in phase. This is seen in Fig. 12(a) where is plotted the height-averaged correlation coefficient between the vegetation velocity and the horizontal flow velocity obtained in Eq. (31). Worth less than 0.1 at $U_R = 0$ the correlation increases
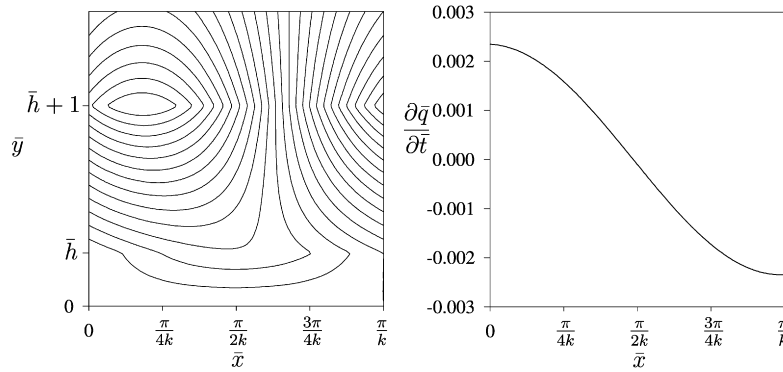
Fig. 10. Streamlines of the water flow and velocity of the plants at $\bar{y} = \bar{h}$ over half a wavelength for $U_R = 0.01$ (outside lock-in).
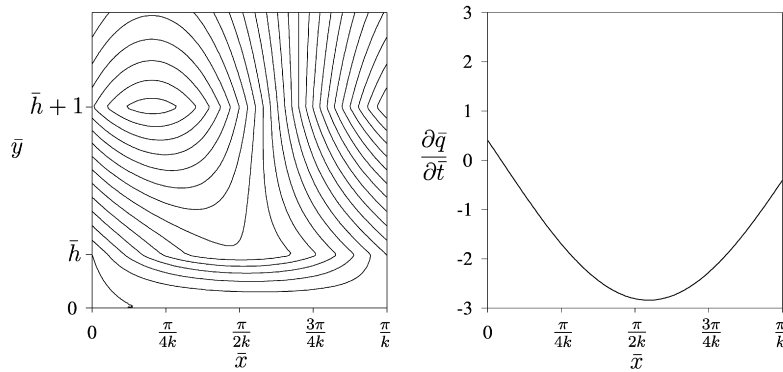

Fig. 11. Streamlines of the water flow and velocity of the plants at $\bar{y} = \bar{h}$ over half a wavelength for $U_R = 0.56$ (within lock-in).

sharply inside the lock-in range. (ii) As in the wind-crop system again, this increase in the coherence between the motion of the vegetation and that of the fluid has for effect to increase the amplitude of $\partial \bar{q} / \partial \bar{t}$ by more than three orders of magnitude between $U_R = 0.01$ and $U_R = 0.59$ for the same perturbation flow energy in Figs. 10, 11. The motion of the plants becomes much more important in the dynamics of the system. (iii) Thirdly, in a manner much more pronounced than for the wind-crop system, the flow inside the aquatic plant canopy is much faster in the lock-in range than at low U_R. In Fig. 11, the streamlines inside the canopy are much closer to one another than in Fig. 10. We see in Fig. 12(b) that as the reduced velocity increases from 0 to 0.5, the percentage of all the fluid perturbation kinetic energy which is located inside the canopy increases steeply from 6% to 29%; a little less than the 35% of the pure configuration. This steep increase matches the surge of the correlation between the motion of the plants and the flow in Fig. 12(a).

Again as in the wind-crop system, the instability confined to the flow at low reduced velocity spreads to the aquatic plants in the lock-in range. As is shown with the following energy analysis, the dynamics of the plants is then responsible for increasing the growth rate of the instability. The increase of $\bar{\omega}_i$ with U_R is plotted in Fig. 13 in solid line along with the two terms of Eq. (28) that accounts for it: the production of kinetic energy by the work of the Reynolds stress against the shear ($\hat{P}_s / 2\hat{E}$) in dash-dot-dot line and the drag dissipation ($\hat{D}_i / 2\hat{E}$) in dotted line. Note that because the Froude number is low in all simulations, the energy stored in the deformation of the free surface ($\hat{S}_f / 2\hat{E}$) is found to be negligible.

The increase of the growth rate with U_R in Fig. 13 is caused by an intensification of the production of perturbation kinetic energy $\hat{P}_s / 2\hat{E}$ and a diminution of the drag dissipation $\hat{D}_i / 2\hat{E}$. The sharp increase of $\hat{P}_s / 2\hat{E}$ is a result of more coherence in the mixing layer $\bar{h} < \bar{y} < \bar{h} + 1$. In Fig. 14, is plotted the distribution with height of the correlation coefficient of the streamwise and verti-
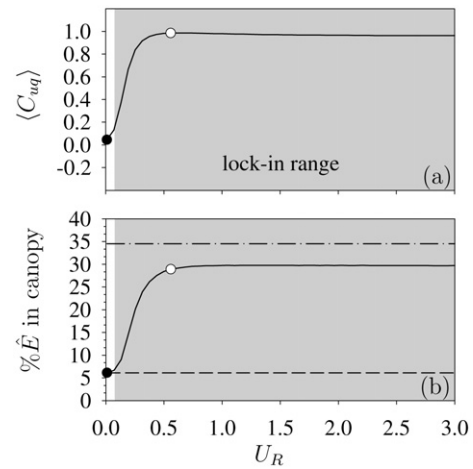

Fig. 12. Correlation of the horizontal water flow and canopy velocities and percentage of the fluid perturbation kinetic energy inside the canopy for increasing reduced velocity in the aquatic plant system: the pure configuration ($- \cdot - \cdot$); the heavy configuration ($- - -$); the coupled configuration ($—$). The grey area marks the lock-in range. The black and the white dots correspond to the cases $U_R = 0.01$ and $U_R = 0.56$ studied in Figs. 10, 11 and 14.

cal perturbation velocities $-C_{uv}(\bar{y})$ obtained in Eq. (30) for a case with small reduced velocity ($U_R = 0.01$ in dash line) and one maximising the growth rate ($U_R = 0.56$ in solid line). The increase in reduced velocity has a substantial effect on the coefficient where it is most significant: inside the mixing layer. The rise with U_R in the correlation between the streamwise and vertical perturbation velocity components has for effect to make the perturbation flow more effective at extracting energy from the mean flow and thus causes the hike of $\hat{P}_s / 2\hat{E}$ in Fig. 13. On the other hand, the decrease of the dissipation $\hat{D}_i / 2\hat{E}$ in Fig. 13 is due to the fluid inside the canopy and the vegetation moving in phase with one another,
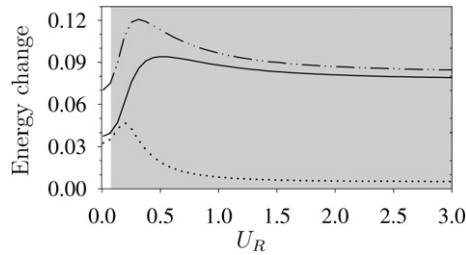
Fig. 13. Energy analysis of the coupled configuration for the aquatic plant system: $\hat{D}_i/2\hat{E}$ ($\cdots\cdots$); $\hat{P}_s/2\hat{E}$ (—··—··); $\bar{\omega}_i$ (—). The grey area marks the lock-in range.
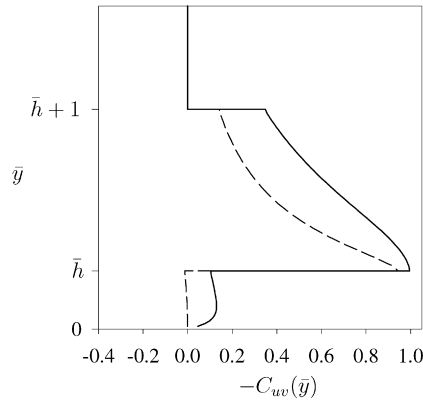
Fig. 14. Height distribution of the correlation coefficient of the streamwise and vertical perturbation velocities in the aquatic plant system for two cases: low reduced velocity, $U_R = 0.01$ (– – –); in the lock-in range, $U_R = 0.56$ (—).

i.e. it is due to the increased height-averaged correlation coefficient $\langle \bar{C}_{uq} \rangle$ with U_R shown in Fig. 12(a).

We may therefore state that for both the wind-crop system and the aquatic plant system, two mechanisms are responsible for further destabilising the flow in the lock-in reduced velocity range: (i) by moving in phase, the flow and the vegetation canopy diminish their interaction and decrease the drag dissipation; and (ii) as the two components of the perturbation fluid flow are more correlated in the mixing layer above the canopy, the perturbation flow is more efficient at extracting energy from the mean flow. The lock-in mechanisms are the same in both systems, but from a glance at Figs. 3 and 9, there are obvious differences in the behaviour of both systems. In the next subsection we explain some of these differences with a dimensionless analysis.

3.4. Dimensionless number analysis

In the wind-crop system, the lock-in velocity range is finite and sharp. The step in the frequency and the bump in the growth rate of the wind-crop system can be seen on the curves identified "S1" in Fig. 15. At low and high reduced velocities, the most unstable frequency is the one related to the KH instability while for the finite lock-in reduced velocity range, the most unstable frequency deviates from that of the KH instability to match the natural frequency of the oscillating canopy. In the case of the aquatic flow over submerged vegetation (shown as "S2" in Fig. 15), past $U_R = 0.2$, the slope of the frequency curve changes and the growth rate increases abruptly. The growth rate peaks when the frequency of the coupled system is merely a quarter of that of the natural frequency of the plants. Moreover, the lock-in perpetuates over a very long reduced velocity range as the most unstable frequency does not return to the KH instability frequency at higher reduced velocities and the growth rate stays high.

It is mainly the mass number M that is responsible for the differences in the size of the lock-in reduced velocity range and the
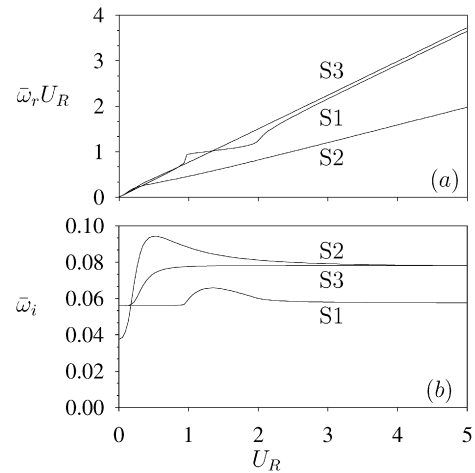
Fig. 15. Comparisons of the frequency (a) and growth rate (b) for 3 different systems: S1 and S2 are the wind-crop and the aquatic plant systems with parameter values given in Table 1, while S3 is a variation of the wind-crop system with the value M of the aquatic plant system.

frequency at which lock-in occurs between the wind-crop and the aquatic plant systems. In Table 1 we see that in the aquatic plant system, the plant-to-fluid mass ratio is much smaller than for the wind-crop system. To comprehend the effects of M on the lock-in mechanism, a simulation is performed on a variation of the wind-crop system using the mass number M of the aquatic plant system. The curves of the frequency and growth rate of this system plotted in Fig. 15 are labelled "S3".

Comparing with the wind-crop system frequency (S1 in Fig. 15(a)) we see that decreasing M (S3 in Fig. 15(a)) completely "smooths out" the frequency lock-in "step" at the natural frequency of the vegetation canopy. It also decreases the lower bound velocity and increases the higher bound velocity of the lock-in range in Fig. 15(b). In fact, for high reduced velocities, the growth rate of the wind-crop system with low M and that of the aquatic plant system (S2 in Fig. 15(b)) are very similar and do not decrease as the lock-in perpetuates.

These results concord with the analysis done by [13] (explained with more details in [22]) with an elementary lock-in model in which the fluid flow and the canopy are modelled as two simple linear oscillators coupled through their velocity difference. This model which captures the essence of the lock-in phenomenon shows that if the fluid oscillator is much heavier than the solid one, the frequencies of the coupled system are simply very close to those of the decoupled oscillators. The most unstable frequency of the wind-crop system with low M (S3 in Fig. 15(a)) is essentially that of the fluid instability.

Concerning the increase of the lock-in reduced velocity range caused by a diminishing mass number, a parallel can be drawn with vortex-induced vibrations. The reduced velocity range over which the shedding frequency in the wake of a freely oscillating bluff body locks onto that of the body is significantly increased by diminishing the mass ratio [23,16]. In vortex-induced vibrations, for small enough mass ratio, lock-in persists up to infinite reduced velocity similarly to what we observe here for the aquatic plant system and the wind-crop system with low M. Note that here our observations on the lock-in range are based on an analysis of the growth rate rather than on the frequency as in Williamson and Govardhan [23].

3.5. Comparison with experiments

To strengthen the findings of this study, two comparisons are made with experimental results. First, we look at the increase of
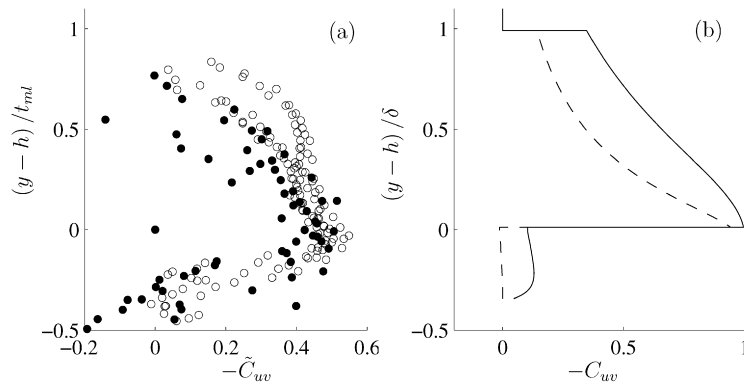
Fig. 16. Comparison of the height distribution of the correlation coefficient of the streamwise and vertical fluctuations in the flow over model aquatic plants (a) measured in the flume experiments of [11] and (b) simulated with the model derived in Section 2. The experimental data comes from 9 runs: 5 where monami was observed marked with ○, and 4 where monami was not observed marked with ●. Two cases are mode led: low reduced velocity, $U_R = 0.01$ (- - -); in the lock-in range, $U_R = 0.56$ (—).

the correlation in the perturbations of the mixing layer and secondly we evaluate the ability of our model to predict monami. For the purpose of comparison, we use the data from the flume experiments on flexible model vegetation of Nepf and Vivoni [18] and Ghisalberti and Nepf [11]. In both of these experimental studies, the time-averaged velocity profile has been measured using a Doppler velocimeter. Binary (yes/no) visual observations were made regarding the occurrence of monami in the aquatic vegetation. The properties of the model aquatic plants are known.

The increase of correlation inside the mixing layer at lock-in predicted by the model in Fig. 14 can be observed in the flume experiments of Ghisalberti and Nepf [11]. In these experiments, the velocity components of the flow were measured in 9 experimental runs. From these measurements Ghisalberti and Nepf [11] calculated the vertical profiles of the correlation coefficient of the streamwise and vertical turbulent fluctuations according to the definition of Eq. (29). We reproduce in Fig. 16(a) the correlation coefficient profiles with a different height scaling. The dimensionless height used in this plot, $(y-h)/t_{ml}$ is measured from the top of the deformed canopy and scaled by the thickness of the mixing layer (t_{ml}). In Fig. 16(a), the correlation profiles of the 9 experimental runs are superimposed: 5 experimental runs where monami was observed are marked with white dots, and 4 experimental runs where monami was not observed are marked with black dots. In Fig. 16(b), the correlation profiles predicted by the model in the lock-in range are plotted in solid line and at low reduced velocity in dash line.

What we can see in Fig. 16(a) is that for all runs, the maximum correlation takes a similar value and is reached at the top of the canopy, $(y-h)/t_{ml} = 0$. This is in agreement with the prediction of our model in Fig. 16(b). Also in Fig. 16(a), although there is scattering, we can see that on average, the correlation decline above the zero height is slower for the runs with monami (white dots) than for the runs without monami (black dots). In Fig. 16(b) it can be seen that the decline of the correlation above $(y-h)/\delta = 0$ is slower for the case inside the lock-in range than the for the one outside lock-in. Note that similar trends are observable in the experimental results if a different scaling using the momentum thickness and/or the height of the inflexion point in the velocity profile is used.

On the other hand, one can notice that in the experiments a maximum correlation around 0.5 was calculated while the model predicts correlations reaching a near perfect 1. This can be explained by the fact that in the current study, the model considers only the most unstable wavelength where in the experiments, a full spectrum of fluctuations are measured.

For the second and last comparison with experimental observations, we test the ability of our model to predict monami in

the flume experiments of Nepf and Vivoni [18] and Ghisalberti and Nepf [11]. Using the same approach as in Section 3.3, the geometry and properties of the flexible vegetation are input (see Appendix B) in the model while considering added mass and buoyancy along with the measured height of water and velocity flow profiles which are fitted on broken-line velocity profiles for the 15 experimental runs described in Nepf and Vivoni [18] and Ghisalberti and Nepf [11].

In order to enable our model to make predictions regarding the occurrence of monami, we must define a criteria to quantify mathematically the physical phenomenon of monami. To do this, we base our reasoning on the observation of Py et al. [13] who showed that the lock-in mechanism explains the coherent wave-motion of the vegetation canopy, and our own observation from Sections 3.2, 3.3 that in the lock-in reduced velocity range, the plant dynamics further destabilises the coupled fluid-structure system. We thus define the intensity of monami as the computed growth rate for the coupled configuration minus the computed growth rate for the heavy configuration $\bar{\omega}_i|_{coupled} - \bar{\omega}_i|_{heavy}$. This criteria gives us a measure of how much more unstable the system is due to the moving canopy. We calculate the correlation between our criteria and the binary observations, B_n, of monami in the $N = 15$ experimental runs of Nepf and Vivoni [18] and Ghisalberti and Nepf [11]

$$C_{B\omega} = \frac{\sum_n^N B_n (\bar{\omega}_i|_{coupled} - \bar{\omega}_i|_{heavy})_n}{[\sum_n^N B_n^2]^{1/2} [\sum_n^N (\bar{\omega}_i|_{coupled} - \bar{\omega}_i|_{heavy})_n^2]^{1/2}}. \tag{32}$$

We find a correlation $C_{B\omega} = 0.8$. This good correlation gives us confidence in the understanding of the interaction mechanisms brought by our linear model coupling a KH instability with an oscillating canopy.

4. Conclusion

This model is obviously not meant as a complete simulation of the complex interactions between flow and a plant canopy. It has evident limitations: It describes highly non-linear phenomena and fluctuations of large amplitudes with a linear theory. It relies on the hypothesis that the most linearly unstable mode is the one which will dominate the dynamics. Its mean velocity profile is highly idealised and except for the crucial inflexion point, does not represent a realistic profile. It does not consider static plant deflection nor 3-dimensional effects. This is not an exhaustive list, but the point is that despite all these limitations, and also thanks to these limitations, this simple model can achieve its goal of singling out the effects due to the coupling of the dynamics of the plants with that of a mixing-layer flow.

For both the wind-crop system and the aquatic plant system, the instability confined to the flow at low reduced velocity spreads

to the vegetation canopy in the lock-in range. The dynamics of the plants is shown to be responsible for increasing the growth rate of the coupled instability in the lock-in range through two mechanisms: (i) because the flow and the vegetation canopy move in phase and thus minimise their interactions the drag dissipation is decreased; (ii) the correlation between the two components of the perturbation flow velocity in the mixing layer is increased and make the perturbation flow more efficient at extracting energy from the mean flow. The later effect is observable in the experiments of Ghisalberti and Nepf [11].

It is shown that the proportion of all the perturbation kinetic energy located inside the canopy is increased in the lock-in range. This increase of the kinetic energy inside the canopy would be associated with increased mixing and fluctuations in a real canopy flow.

Despite its simplicity, the coupled model shows that none of the crucial physical components have been discarded out by offering monami predictions well correlated with experimental observations. This increases the confidence in the understanding of the interaction mechanism brought by the model used in this article.

The effects free-surface boundary conditions have on the model have not been systematically studied. The parameters used in the simulations were chosen so as to minimise the effects of the free-surface. The free surface can affect the dynamics obviously through coupling with surface waves but also by acting as a confining ceiling to the KH instability. It was shown by Huerre [24] that confinement has a stabilising effect on mixing layers. Studying this confinement effect could push further the understanding brought by experimental observations and phenomenological models on the limited growth of shear layers in aquatic vegetation [11,25].

Acknowledgements

Appendix A. Analytical solution

Upon substitution of the travelling-wave solution in Eqs. (9)–(11), we can solve analytically for the general shape functions of the vertical velocity and pressure fields in the domain: for $\bar{y} \leqslant \bar{h}$

$$\hat{v}(\bar{y}) = A_1 e^{\kappa \bar{y}} + A_2 e^{-\kappa \bar{y}} - \frac{i\bar{\omega}C}{k^2(1 - R - \bar{\omega}/\bar{k})} \frac{\partial \chi}{\partial \bar{y}} \hat{q}, \tag{A.1}$$

$$\hat{p}(\bar{y}) = -i\left(1 - R - \frac{\bar{\omega}}{\bar{k}} - i\frac{C}{\bar{k}}\right)\frac{\kappa}{\bar{k}}\left(A_1 e^{\kappa \bar{y}} - A_2 e^{-\kappa \bar{y}}\right) - \frac{\bar{\omega}C}{\bar{k}} \chi \hat{q}, \tag{A.2}$$

for $\bar{h} \leqslant \bar{y} \leqslant \bar{h} + 1$

$$\hat{v}(\bar{y}) = A_3 e^{\bar{k}\bar{y}} + A_4 e^{-\bar{k}\bar{y}}, \tag{A.3}$$

$$\hat{p}(\bar{y}) = -i\left[1 + 2R\left(\bar{y} - \bar{h} - \frac{1}{2}\right) - \frac{\bar{\omega}}{\bar{k}}\right]\left(A_3 e^{\bar{k}\bar{y}} - A_4 e^{-\bar{k}\bar{y}}\right) + \frac{i2R}{\bar{k}}\left[A_3 e^{\bar{k}\bar{y}} + A_4 e^{-\bar{k}\bar{y}}\right], \tag{A.4}$$

and for $\bar{h} + 1 \leqslant \bar{y}$

$$\hat{v}(\bar{y}) = A_5 e^{\bar{k}\bar{y}} + A_6 e^{-\bar{k}\bar{y}}, \tag{A.5}$$

$$\hat{p}(\bar{y}) = -i\left(1 + R - \frac{\bar{\omega}}{\bar{k}}\right)\left[A_5 e^{\bar{k}\bar{y}} - A_6 e^{-\bar{k}\bar{y}}\right], \tag{A.6}$$

where $\kappa = \bar{k}(1 - R - \bar{\omega}/\bar{k})^{\frac{1}{2}}(1 - R - \bar{\omega}/\bar{k} - iC/\bar{k})^{-\frac{1}{2}}$, and $A_1, A_2, \ldots, A_6$ are constants. In [13], because of the irrotational flow assumption (discussed at the end of Section 2.1 and in Section 3.1), $\kappa = \bar{k}$ in Eqs. (A.1)–(A.2) and the $\hat{q}$ term in Eq. (A.1) disappears. These simplifications allow them to obtain a dispersion relation in the form of a polynomial.

The constants $A_1, A_2, \ldots, A_6$ can be evaluated by enforcing two sets of conditions: (i) that the vertical velocity and pressure shape functions be continuous over the entire $\bar{y}$-domain

$$\hat{v}|_{\bar{y}=\bar{h}^-} = \hat{v}|_{\bar{y}=\bar{h}^+}, \qquad \hat{v}|_{\bar{y}=(\bar{h}+1)^-} = \hat{v}|_{\bar{y}=(\bar{h}+1)^+},$$
$$\hat{p}|_{\bar{y}=\bar{h}^-} = \hat{p}|_{\bar{y}=\bar{h}^+}, \qquad \hat{p}|_{\bar{y}=(\bar{h}+1)^-} = \hat{p}|_{\bar{y}=(\bar{h}+1)^+}, \tag{A.7}$$

and (ii) that the solution satisfies the boundary conditions equations (4) in dimensionless travelling-wave form

$$\hat{v}|_{\bar{y}=0} = 0, \qquad \lim_{\bar{H}_b \to \infty} \hat{v}|_{\bar{y}=\bar{H}_b} = 0. \tag{A.8}$$

We substitute the travelling-wave solution in the oscillator equation (12), and after integrating by parts the analytical flow solution we get

$$\left[\bar{r} - \bar{\omega}^2 \bar{m} - i\frac{1}{3}C_D d(1 - R)\bar{\omega}h\right]\hat{q}$$
$$= iC_D(1 - R)\frac{d}{h\bar{k}}\left[A_1\left(h - \frac{1}{\kappa}\right)e^{\kappa h} + \frac{A_1}{\kappa}\right.$$
$$\left. + A_2\left(h + \frac{1}{\kappa}\right)e^{-\kappa h} - \frac{A_2}{\kappa}\right]. \tag{A.9}$$

We rewrite the seven Eqs. (A.7), (A.8) and (A.9) as a linear operator of the seven constants $A_1, A_2, A_3, A_4, A_5, A_6$ and $\hat{q}$ to obtain Eq. (14).

Appendix B. Modelling aquatic plants

B.1. Modal mass and natural frequency of the model aquatic plants

We consider a model plant as a vertical cantilevered beam of Young's modulus E, moment of inertia I, length L, mass per unit length m_1, with uniform cross-section; the equation of motion of its lateral oscillation in a dense fluid is given by

$$EI\frac{\partial^4 Q}{\partial y^4} + (m_1 + m_2)\frac{\partial^2 Q}{\partial t^2} - \frac{\partial}{\partial y}\left(T\frac{\partial Q}{\partial y}\right) = 0,$$

where m_2 is the added mass of fluid oscillating with the beam and the tension in the beam is given by

$$T(y) = g(A\rho - m)(L - y),$$

where g is the gravitational acceleration, A the cross-sectional area of the beam and ρ is the density of the surrounding fluid. We can estimate the added mass per unit length of the model plant as being that of a flat section [26, p. 25], i.e.,

$$m_2 = \rho\pi\frac{w^2}{4},$$

Table B.1
Values of parameters taken and computed from [11] and [18]

Study	w (mm)	T (mm)	A (m^2)	I (m^4)	E (Pa)	L (m)	ρ_s (kg/m^3)
G. & N. 2002	3	0.1	3E−7	2.5E−16	0.30E9	0.127	920
N. & V. 2000	3	0.25	7.5E−7	39.0 E−16	2.56E9	0.14	950

where w is the width of the model plant. We use Galerkin's method [27] to find the lowest cantilevered beam frequency of the system. With the parameters of Ghisalberti and Nepf [11] and Nepf and Vivoni [18] given in Table B.1, the natural frequency of each model plant and its effective modal mass (taking into account added mass and buoyancy) can be calculated. Note that in both experimental studies, the model plants had a wooden dowel at their base to mimic the eelgrass stem. The height added by this dowel is subtracted from the height of the plants used in our calculations since it does not deform. By taking the height of the plants smaller, we model a mixing layer that is closer to the ground than it really is, but this is a limitation of our model with a broken-line velocity profile (see Fig. 1).

B.2. Fitting the broken line profile on experimental measurements

In the paper by Ghisalberti and Nepf [11], the model plants underwent large amplitude deformation (both static and dynamic). Since our analytical model cannot account for large deformations, the height of the canopy h is taken as the average deformed height measured minus the height of the wooden dowel (discussed in the previous subsection). The hyperbolic tangent velocity profiles $U_{\text{tanh}}(y)$ measured with an Acoustic Doppler velocimeter are fitted on the broken-line profile $U_b(y)$ (see Fig. 1). To do this, we have to impose three similarity conditions. First, the mean velocity is the same in both profiles:

$$U = \bar{U}_{\text{tanh}}. \tag{B.1}$$

Secondly, the velocity inside the canopy is equal to the average of that in the hyperbolic tangent profile:

$$U_2 = \frac{1}{h} \int_0^h U_{\text{tanh}}(y)\, dy. \tag{B.2}$$

Lastly, in order to scale the thickness of the mixing layer, we assume that both profiles have the same KH instability frequency in an unbounded domain, i.e.,

$$f_{\text{tanh}} = f_{\text{B.L.}}, \tag{B.3}$$

where the frequency of the hyperbolic tangent profile is related to the momentum thickness θ_{tanh}: $f_{\text{tanh}} = 0.032 \bar{U}_{\text{tanh}}/\theta_{\text{tanh}}$ [12] and the frequency of the broken lines profile $f_{\text{B.L.}} = 0.8 U / 2\pi\delta$ is found by finding the dispersion relation of the fluid system obtained by integrating Eqs. (9)–(11) in an infinite domain while discarding the drag/coupling term.

To find the drag coefficient of the model plants, the y-dependent frontal area per volume (canopy density) and drag coefficients of Fig. 3 in Nepf and Vivoni [18] are integrated over the plant height. The drag coefficient for the Ghisalberti and Nepf [11] runs was assumed to be the same as in Nepf and Vivoni [18].

References

[1] E. de Langre, Effects of wind on plants, Annual Review of Fluid Mechanics 40 (2008) 141–168.

[2] B.A. Gardiner, The interactions of wind and tree movement in forest canopies, in: M. Couts, J. Grace (Eds.), Wind and Trees, Cambridge University Press, Cambridge, 1995.

[3] S. Dupont, Y. Brunet, Simulation of turbulent flow in an urban forested park damaged by a windstorm, Boundary-Layer Meteorology 120 (2006) 133–161.

[4] P.M. Berry, M. Sterling, J.H. Spink, C.J. Baker, R. Sylvester-Bradley, S.J. Money, A.R. Tams, A.R. Ennos, D.L. Sparks, Understanding and reducing lodging in cereals, Advances in Agronomy 84 (2004) 217–271.

[5] M.R. Raupach, A.S. Thom, Turbulence in and above plant canopies, Annual Review of Fluid Mechanics 13 (1981) 97–129.

[6] J. Finnigan, Turbulence in plant canopies, Annual Review of Fluid Mechanics 32 (2000) 519–571.

[7] M. Ghisalberti, H. Nepf, The structure of the shear layers in flows over rigid and flexible canopies, Environmental Fluid Mechanics 6 (2006) 277–301.

[8] J. Diener, L. Reveret, E. Fiume, 2006. Hierarchical retargetting of 2d motion fields to the animation of 3d plant models, in: ACM-SIGGRAPH/EG Symposium on Computer Animation. Eurographics Association, Aire-la-Ville, Switzerland, pp. 187–195.

[9] B. Moulia, D. Combes, 2006. Thigmomorphogenetic acclimation of plants to moderate winds as a major factor controlling height growth and biomass distribution in crops, as demonstrated in alfalfa (medicago sativa l.), in: Proceedings of the 5th Plant Biomechanics Conference. STFI, Stockholm, pp. 317–322.

[10] M.R. Raupach, J.J. Finnigan, Y. Brunet, Coherent eddies and turbulence in vegetation canopies: The mixing-layer analogy, Boundary-Layer Meteorology 78 (1996) 351–382.

[11] M. Ghisalberti, H.M. Nepf, Mixing layers and coherent structures in vegetated aquatic flows, Journal of Geophysical Research 107 (2002) 3011.

[12] C. Ho, P. Huerre, Perturbed free shear layers, Annual Review of Fluid Mechanics 16 (1984) 365–422.

[13] C. Py, E. de Langre, B. Moulia, A frequency lock-in mechanism in the interaction between wind and crop canopies, Journal of Fluid Mechanics 568 (2006) 425–449.

[14] T. Farquhar, C. Eggleton, Pulsatile flow heightens vertical exchanges in a wheat canopy, in: Proceedings of the 3rd Plant Biomechanics Conference, Freiburg, Germany, Georg Thieme Verlag, Stuttgart, Germany, 2000, pp. 529–536.

[15] O. Doaré, B. Moulia, E. de Langre, Effect of plant interaction on wind-induced crop motion, Journal of Biomechanical Engineering 126 (2004) 146–151, pMID: 15179844.

[16] E. de Langre, Frequency lock-in is caused by coupled-mode flutter, Journal of Fluids and Structures 22 (2006) 783–791.

[17] C. Py, E. de Langre, B. Moulia, The mixing layer instability of wind over a flexible crop canopy, Comptes Rendus de Mécanique 332 (2004) 613–618.

[18] H.M. Nepf, E.R. Vivoni, Flow structure in depth-limited, vegetated flow, Journal of Geophysical Research 105 (2000) 28527–28546.

[19] P.G. Drazin, W.H. Reid, Hydrodynamic Stability, Cambridge University Press, Cambridge, 1981.

[20] C. Cossu, L. Brandt, On Tollmien–Schlichting-like waves in streaky boundary layers, European Journal of Mechanics B: Fluids 23 (2004) 815–833.

[21] H. Tennekes, J.L. Lumley, A First Course in Turbulence, MIT Press, Cambridge, MA, 1972.

[22] C. Py, Couplage entre la dynamique du vent et le mouvement d'un couvert végétal., Ph.d, Thesis, LadHyX, École Polytechnique, Palaiseau, France, 2005.

[23] C.H. Williamson, R. Govardhan, Vortex-induced vibrations, Annual Review of Fluid Mechanics 36 (2004) 413–455.

[24] P. Huerre, Finite amplitude evolution of mixing layers in the presence of solid boundaries, Journal de Mécanique Théorique et Appliquée Numéro Spécial (1983) 121–145.

[25] M. Ghisalberti, H.M. Nepf, The limited growth of vegetated shear layers, Water Resources Research 40 (2004) 3011, W07502.

[26] R. Blevins, Flow-Induced Vibration, Van Nostrand Reinhold, New York, 1977.

[27] R.E.D. Bishop, D.C. Johnson, The Mechanics of Vibration, Cambridge University Press, Cambridge, 1960.